Nonlinear Dyn
https://doi.org/10.1007/s11071-025-11424-5

RESEARCH

# Dynamical integrity of periodic orbits: a computationally efficient approach

**Dóra Patkó · Giuseppe Habib**

Received: 28 March 2025 / Accepted: 25 May 2025

**Abstract** The dynamical integrity of a solution in a dynamical system reflects its robustness against external perturbations, with a larger basin of attraction indicating greater robustness. However, computing the entire basin of attraction can be computationally expensive. The local integrity measure offers an efficient alternative by quantifying the compact region of the basin of attraction around the steady state of interest. Recently, a rapid algorithm was introduced to estimate the dynamical integrity of equilibrium points using the local integrity measure. This paper extends this method to estimate the dynamical integrity of stable periodic orbits in both autonomous and periodically excited systems. The enhanced algorithm, implemented in the `DynIn MATLAB` Toolbox, is evaluated on four engineering systems; specifically, a Duffing–van der Pol oscillator with an attached tuned mass damper, a pitch-and-plunge wing profile, a harmonically excited Duffing oscillator, and a passive vertical hopping model. The results demonstrate that the algorithm is both rapid and effective, yielding meaningful engineering insights and paving the way for incorporating dynamical integrity as a design parameter.

**Keywords** Basin stability · Dynamical integrity · Limit cycle oscillation · DynIn MatLab toolbox · Local integrity measure · Numerical algorithm

## 1 Introduction

One of the major challenges of a nonlinear dynamical system is that the stability of a steady-state solution does not guarantee its global stability, as it may have limited robustness against external perturbations. This means that while a system in a stable state will return to its original state after a small perturbation, a sufficiently large perturbation may cause it to diverge or converge toward an alternative, typically undesired, solution. The ability of a steady state to persist under external perturbations is commonly referred to as dynamical integrity [1,2] or basin stability [3].

This issue arises in many practically relevant systems. For instance, in wheel shimmy, a wheel in equilibrium can suddenly diverge towards shimmy oscillations after a perturbation [4,5]. Similarly, even at flow velocities considered safe in wing flutter, perturbations due to gusts can trigger stable flutter oscillations [6,7]. In robot control, limited dynamical integrity of a desired state may cause the controller to drive the system toward an undesired configuration [8]. For floating bodies, almost any structure subjected to an excessively

D.Patkó (✉)· G.Habib
Department of Applied Mechanics, Faculty of Mechanical Engineering, Budapest University of Technology and Economics, Műegyetem rkp. 3., H-1111 Budapest, Hungary
email:dora.patko@mm.bme.hu

D.Patkó · G.Habib
MTA–BME Lendület “Momentum” Global Dynamics Research Group, Budapest University of Technology and Economics, Műegyetem rkp. 3., Budapest 1111, Hungary

large perturbation risk capsizing, a concerning issue for some types of floating wind turbines [9], for example. These are just a few examples of a broad problem affecting very diverse systems, including power grids [10], epidemiological models [11], and ecological systems [12], to name a few.

The dynamical integrity of an attractor can be studied through its basin of attraction (BoA), which is the set of all initial conditions in the phase space that asymptotically lead to that attractor. The larger the basin of attraction, the more robust the steady state.

Several methods exist for computing BoAs. However, analytical approaches are often difficult or even infeasible to implement [13,14], while numerical methods are computationally expensive [15–17]. Probably the most efficient approach is the cell-mapping method [18,19], whose basic idea is to consider the state space not as a continuum but as a collection of state cells, with each cell taken as a state entity. Despite the remarkable results obtained with this method, it remains computationally prohibitive for high-dimensional systems (issue mitigated only through heavy parallel computation [20,21]) and suffers from memory limitations.

An alternative approach to studying the dynamical integrity of a steady state without explicitly computing its BoA consists of performing several simulations with random initial conditions and determining the fraction of simulations that lead to the desired solution. This procedure estimates the so-called basin stability [3], corresponding to the global integrity measure [22]. However, this measure does not account for the fractal and intermingled nature of large portions of a system's BoA. As a result, a solution may appear robust based on a high basin stability despite its BoA being largely fractal and, therefore, unsafe.

A different approach, introduced in [23], does not attempt to compute the entire BoA but instead estimates the local integrity measure (LIM), i.e., a measure [1] that quantifies the dynamical integrity of a steady state through a scalar quantity. The LIM is defined as the radius of the largest hypersphere centered at the steady state and entirely included within the solution's BoA; therefore, it automatically excludes fractal regions and focuses on the compact and safe portion of the BoA, in line with the concept of the safe basin [24]. By sacrificing full BoA knowledge, this algorithm significantly reduces computational costs while delivering a single scalar value that quantifies the dynamical integrity of a steady state. Additionally, unlike the integrity factor [24], the LIM is more manageable to compute, requiring only a simple distance calculation between the attractor and the BoA boundaries.

The algorithm proposed in [23], implemented in the `DynIn MATLAB` Toolbox, iteratively refines the estimated LIM by restricting the compact portion of the BoA to the region marked by the current LIM estimate. At each iteration, a new trajectory is simulated; if the trajectory does not converge to the desired solution, the LIM is recalculated. The key advantage of this approach is its speed, making it suitable for parametric analyses in design applications. Additionally, it is compatible with virtually any type of mathematical model, including ordinary differential equations, difference equations, and black-box models, as long as the system has finite dimensions. It also extends to nonsmooth systems. However, like other dynamical integrity estimation methods, it faces challenges in high-dimensional systems. In [25], the algorithm was further extended to time-delay systems.

A significant limitation of the original algorithm is that it applies only to fixed points or periodic solutions of periodically excited systems, reduced to fixed points through Poincaré stroboscopic map. The present study aims to extend the algorithm to analyze limit cycles of autonomous systems (whose period is unknown a priori) and periodic solutions of periodically excited systems, considering the entire trajectory rather than just its stroboscopic mapping. These extensions require significant modifications to the algorithm in [23], as discussed in Sect. 2. The enhanced algorithm, implemented in the `DynIn` Toolbox, is tested on four different numerical systems of engineering relevance; namely, a Duffing-van der Pol oscillator with an attached tuned mass damper, a pitch-and-plunge wing profile, a harmonically excited Duffing oscillator, and a passive vertical hopping model. For each system, the dynamical integrity is analyzed under various parameter variations, providing insight into how system parameters affect dynamical integrity.

## 2 Algorithm

The core of the algorithm used in this study is essentially the same as presented in [23] and available in the `DynIn` Toolbox. However, several changes had to be implemented because of the qualitative differences between equilibrium points and periodic orbits.

The main differences are discussed below. The following subsections treat periodic orbits of autonomous and periodically excited systems separately.

## 2.1 Local integrity measure for limit cycles

Firstly, the LIM of limit cycles has to be defined; its original definition, provided in [1], is limited to equilibrium points, or Poincaré sections of periodic orbits. It states that the LIM of an equilibrium point is equal to the radius of the largest hypersphere, which is entirely included in the BoA of the solution and centred at it, which we term here hypersphere of convergence. This definition is extended to periodic orbits, as the radius of the largest hypersphere that is entirely part of the BoA and centred at any point of the periodic orbit. This results in a hypertorus built around the periodic orbit where convergence is granted. For the numerical procedure implemented, the calculation of the LIM is limited to a finite number of points of the periodic orbit.

### *2.1.1 Identifying limit cycles*

The first step of the computation is the identification of the periodic orbit unless explicitly provided by the user. This is a relatively straightforward operation since the solution must be stable; accordingly, it can be obtained through direct numerical simulations of the system. The algorithm, or optionally the user, defines a Poincaré section, which is expected to intersect the periodic orbit. Then, the algorithm initiates a trajectory from a point presumed to be within the BoA and identifies the directional crossing points of the trajectory on the Poincaré section. Each crossing point is compared to the previous crossing points. If the norm of the distance of any pair of crossing points is less than an error limit, the trajectory between these two points is assumed to be the periodic orbit.

An illustrative example of the periodic orbit identification is shown in Fig. 1. The directional crossing points of the trajectory on the Poincaré section are marked with dots. Since the distance between point VI and point IV is within the error limit, point VI is identified as a point of a stable periodic solution. Within the predefined error limit, the periodic solution is the trajectory between points IV and VI.

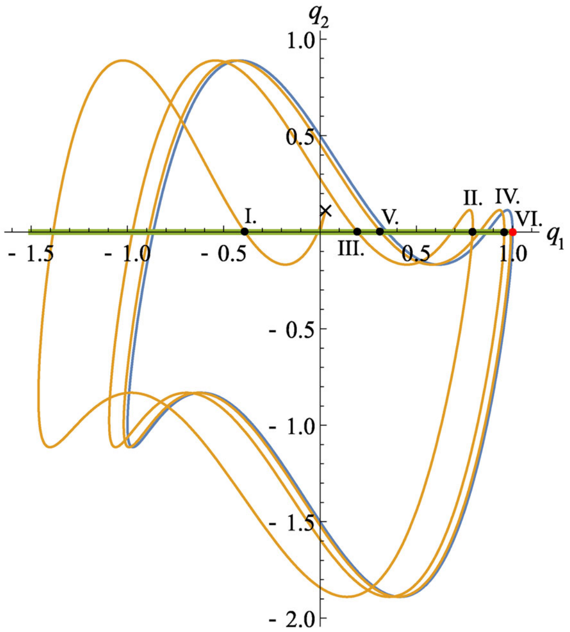

**Fig. 1** Visualisation of the periodic orbit identification, where the sought periodic orbit is the blue curve. The green line is the projection of the Poincaré section onto the $(q_1, q_2)$ phase plane, and the initial condition is denoted by ×. The crossing points of the trajectory (orange curve) on the Poincaré section are denoted with dots numbered in Roman numerals

## 2.2 Local integrity measure for periodic orbits of periodically excited systems

In the case of periodically excited systems, the excitation phase constitutes an additional dimension that must be considered. For the LIM definition, the phase space is divided into infinitely many subspaces, one for each phase $\vartheta \in [0, T)$. Then, for each point of the periodic orbit, limited to its corresponding subspace, the radius of the largest hypersphere centred at that point and entirely included within the BoA is computed. Finally, the LIM is defined as the radius of the smallest hypersphere. For practical computation, only a finite number of phases is considered. Also, in this case, the LIM defines a hypertorus around the periodic orbit within which convergence is guaranteed.

### *2.2.1 Identifying periodic orbits of periodically excited systems*

Opposed to limit cycles, the time period of stable periodic solutions of forced systems typically coincides with the excitation period $T$ and is generally known.

At a given excitation phase, the trajectory of a stable periodic orbit behaves as a fixed point. Accordingly, to identify the periodic solution, it is sufficient to sample a trajectory on a stroboscopic Poincaré map with period $T$ and verify that the distance between two subsequent points is smaller than a given tolerance. The periodic orbit is then given by the portion of the trajectory between these two points. It is important to note that a periodic orbit does not necessarily exist, as discussed later in Sect. 4.2.

## 2.3 Estimating local integrity measure by the DynIn Toolbox

The `DynIn` Toolbox exploits an iterative procedure. For each iteration step, a trajectory is generated, and its converging properties are evaluated. In the case of diverging trajectories, the LIM is recomputed (reduced) as the minimal distance between the trajectory and the periodic solution. Details of the basic working algorithm are thoroughly explained in [23]. In the following sections, the algorithm modified for periodic solutions of autonomous and non-autonomous systems is discussed in detail.

### *2.3.1 Estimating LIM of limit cycles of autonomous systems*

The limit cycle is discretized for autonomous systems into a user-chosen number of points, and the state space of interest is divided into cells. At first, all cells containing points of the periodic orbit are marked as 'converging'. Meanwhile, the other cells will be later classified as either 'converging' or 'non-converging' during the iterative algorithm (and only if reached by one of the computed trajectories, as explained below).

Stable steady-state solutions different from the desired one are identified by examining how often trajectory points fall within the same cell. In particular, if a trajectory remains in the same cell for a given number of consecutive sampling intervals, its computation is interrupted, and its final point is classified as an equilibrium. Cells through which this trajectory passes are then marked as 'non-converging' (concerning the desired solution because they lead to another one). Conversely, if non-consecutive points of a trajectory repetitively pass through the same cell, it is assumed that the trajectory has reached a periodic orbit (different from the desired one); also in this case, the cells containing points of the trajectory are classified as 'non-converging'. Additionally, if a trajectory leaves the phase space of interest, it is immediately classified as 'non-converging', regardless of whether it would eventually have converged to the desired solution. Finally, if a trajectory reaches any cell that has already been classified by a previous trajectory, the numerical integration is interrupted, and the new trajectory is assumed to share the same convergence property, so all cells it crosses are classified accordingly. Extensive details of this classification procedure are available in [23].

The LIM value is updated and decreased if necessary for each non-converging trajectory identified. A visualization of the LIM calculation is shown in Fig. 2. In the figure, the orange line represents a non-converging trajectory leading to the trivial equilibrium. For each analysed point of the periodic orbit, the radius of the hypersphere is computed as the smallest distance between that point and the sampling points of the non-converging trajectory. The smallest calculated radius is then used as the new LIM, which is then reduced iteratively. Defining the distance is not trivial, as the phase space is generally anisotropic; this issue is addressed by applying appropriate weights for each direction in the phase space, as explained in [23]. The newly computed LIM value is compared to the last recorded one at each iterative step, and the smallest is retained.

Initial conditions (ICs) of each trajectory are chosen by using either technique described in [23] – where the ICs are chosen as the estimated farthest point from any other investigated point in the phase space – or through a bisection method as detailed in [25], which aims to initiate trajectories from the boundary of the BoA. The former method provides a more homogeneous phase space analysis, increasing the probability that all existing stable solutions are identified. Conversely, while the latter method is generally faster and more precise, it might overlook some dynamical phenomena of the system. In any case, the ICs are chosen within the estimated hypertorus defined by the LIM or in its vicinity since only trajectories that reduce the LIM are effectively relevant for its accurate estimation.

### *2.3.2 Estimating LIM of limit cycles of periodically excited systems*

As mentioned above, in the case of periodically excited systems, the phase space is divided into a finite number

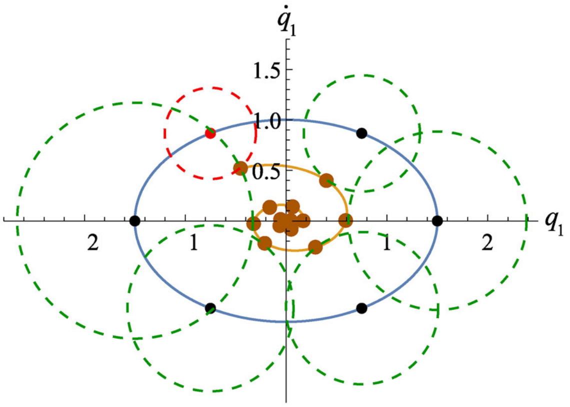

**Fig. 2** Visualisation of the projection of estimated hyperspheres (dashed circles) onto $(q_1, \dot{q}_1)$ plane for each discretized point of the periodic orbit (blue curve). Orange dots denote the sampling points of the non-converging trajectory. The radius of the red circle around the red point of the limit cycle defines the LIM

$N_\mathrm{T}$ of subspaces; each trajectory sequentially crosses all subspaces once per excitation period. Each subspace is further divided into the same number of cells, and all cells containing points of the periodic solution at the respective phases are marked as ‘converging’. The sampling time of each trajectory is automatically set to $T/N_\mathrm{T}$ to align with the phase subspaces.

Other stable solutions are identified by tracking cell repetitions, similarly to the case of autonomous systems, as explained in Sect. 2.3.1. However, in this case, a different set of cells is related to each phase. Because of the periodic excitation, periodic solutions of period $T$ are reduced to a finite number of fixed points in each subspace, typically a single point unless period-doubling phenomena occur; quasiperiodic solutions, on the other hand, appear as closed curves in each subspace. Excluding trivial cases, the system cannot have equilibrium points. Accordingly, if a trajectory remains within the same cell (of the same subspace) for a number of consecutive time periods, it is assumed to have reached a periodic orbit. Conversely, suppose non-consecutive points of a trajectory pass through the same cell a given number of times. In that case, the trajectory is assumed to have reached a steady-state solution, which may be either periodic after period doubling, quasiperiodic, or chaotic. Although a detailed trajectory analysis could reveal its nature, this distinction is unnecessary for the objectives of the algorithm; thus, these types of solutions are not differentiated. All cells containing points of these trajectories are labelled as ‘non-converging’. If a trajectory leaves the phase space of interest in any of the phases, the simulation is interrupted, and the cells containing its points are marked as ‘non-converging’. It is worth noting that cells at the same position but related to different subspaces may have different converging properties. Finally, suppose a trajectory reaches an already labelled cell. In that case, the simulation is terminated, and the cells containing its points are labelled as either ‘converging’ or ‘non-converging’ according to the convergence properties of the reached cell.

For each non-converging trajectory, the LIM value is recalculated as the minimal distance between the desired solution and the non-converging trajectory computed in each subspace. The LIM value is updated only if it is smaller than the previously recorded value.

## 3 Case studies for autonomous systems

Regarding autonomous systems, the algorithm is tested on two case studies: a Duffing-van der Pol oscillator with a tuned mass damper and a flutter-based energy harvesting wing profile. The results for each example are validated through bifurcation diagrams.

### 3.1 Duffing-van der Pol oscillator with tuned mass damper

The first system analysed in this study is the Duffing-van der Pol oscillator with an attached tuned mass damper (TMD) [26,27]. The equations of motion are given as follows:

$$\begin{cases} \ddot{x}_1 - 2\left(\mu_1 \dot{x}_1 - \gamma \mu_2 r \dot{x}_2\right) + x_1 + \gamma^2 r\, x_2 \\ \quad + \alpha x_1^3 + 2\mu_1 x_1^2 \dot{x}_1 = 0, \\ \ddot{x}_2 - 2\left(\mu_1 \dot{x}_1 - \gamma \mu_2 (1+r) \dot{x}_2\right) + x_1 \\ \quad + \gamma^2 (1+r)\, x_2 + \alpha x_1^3 + 2\mu_1 x_1^2 \dot{x}_1 = 0, \end{cases} \tag{1}$$

where $\alpha$ represents the cubic stiffness, $\mu_1$ indicates the negative damping ratio of the primary system, $\mu_2$ is the damping ratio of the TMD, while $r$ and $\gamma$ denote the mass and natural frequency ratios between the primary system and the TMD, respectively. The generalised coordinates consist of the displacements of the primary system ($x_1$) and TMD ($x_2$). The parameter set utilised for the calculations is presented in Table 1.

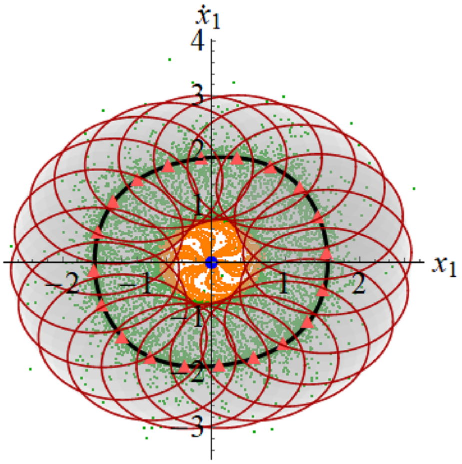

**Fig. 3** Output for Duffing-van der Pol oscillator with an attached tuned mass damper. Solid black curve: examined periodic orbit; red triangles: discretised points of the periodic orbit; grey area: projection of the hypertorus on the phase plane's section $(x_1, \dot{x}_1)$; green dots: sampling points of converging trajectories, orange dots: sampling points of non-converging trajectories; blue dot: other attractor found by the algorithm

The negative damping ratio of the primary system, $\mu_1$, serves as the bifurcation parameter; therefore, it is not included in the table. For further information regarding the physical relevance of the model and the adopted nomenclature, interested readers are referred to [27].

The output of the `DynIn` Toolbox, based on the parameter set provided in Table 1 with $\mu_1 = 0.075$, is depicted in Fig. 3. The stable periodic orbit was discretised into 20 points. Around each point, the projection of the hyperspheres, each with a radius equal to the estimated LIM value of the periodic orbit, is represented by red circles. By translating these hyperspheres along the periodic orbit, we obtain a hypertorus that describes a compact area of the BoA for the solution, as illustrated by the transparent grey area. As shown, the algorithm successfully identified the stable trivial solution of the system, denoted by the blue dot. Moreover, green and orange points in Fig. 3 mark sampling points of converging and non-converging trajectories, respectively.

Let us investigate the system's dynamics as we vary $\mu_1$. According to the bifurcation diagram in Fig. 4a, obtained by combining a shooting technique with a pseudo-arclength continuation, the trivial solution is globally stable for $\mu_1 < 0.0619$. At $\mu_1 = 0.0619$, a fold bifurcation occurs, leading to the coexistence of a stable limit cycle with the stable trivial equilibrium for $\mu_1 \in (0.0619, 0.1005)$, separated by an unstable limit cycle. At $\mu_1 = 0.1005$, the trivial solution becomes unstable due to a subcritical Andronov-Hopf bifurcation, marking the end of the bistable region.

In general, trajectories converge toward the trivial equilibrium when moving inward from the unstable limit cycle and toward the stable limit cycle when moving outward. However, the four-dimensional nature of the system adds complexity to its topology. As the amplitude difference between the stable and unstable limit cycles increases after the fold bifurcation, we anticipate that the LIM of the stable limit cycle will also rise in response to this increasing distance. Additionally, based on the bifurcation diagram in Fig. 4a, from a mathematical standpoint, when the trivial solution is unstable, the LIM should have shown a gradual variation, since the origin becomes an isolated point external to the BoA of the limit cycle within the phase space. However, the algorithm does not account for this singular point, as it requires the system to begin precisely at the origin to be identified. Therefore, we expect not only gradual variation at the Andronov-Hopf bifurcation, but a sudden positive jump in the LIM value. Moreover, from an engineering perspective, the existence of this isolated point is inconsequential to the dynamical integrity of the limit cycle since the probability of trajectories being precisely at the origin is zero. Consequently, isolated points will be excluded from the dynamical integrity analysis in this study.

The LIM value was computed over a range of negative damping ratio values ($\mu_1$) to verify whether its variation aligns with the trend of the amplitude of the unstable limit cycle, as previously discussed. Assuming that the dynamics of the system is not influenced by phenomena not represented in the bifurcation diagram, and presuming that the basins of attraction have regular shapes around the solutions, it is expected that the trend of the LIM is closely related (though not necessarily equal) to the distance between the stable and unstable limit cycles. Therefore, this analysis may validate the effectiveness of the algorithm.

The input values utilised in the `DynIn` Toolbox are presented in Table 2. The meaning of each parameter is provided below:

- `number_of_steps`: this determines the number of iteration steps corresponding to the number of separate simulations the algorithm will perform.
- `spaceboundary`: this parameter marks the dimension of the phase space of interest.

**Table 1** Dimensionless parameter values of the Duffing-Van der Pol oscillator with an attached tuned mass damper

| $r$ | $\gamma$ | $\mu_2$ | $\alpha$ |
|---|---|---|---|
| 0.05 | 0.97 | 0.12 | 0.3 |

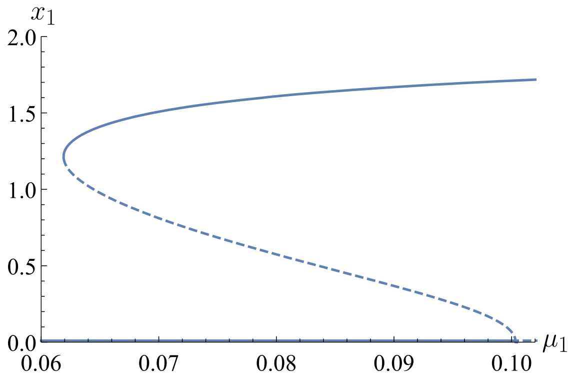

(a) Bifurcation diagram. The amplitude of stable and unstable solutions are denoted by solid and dashed lines, respectively.

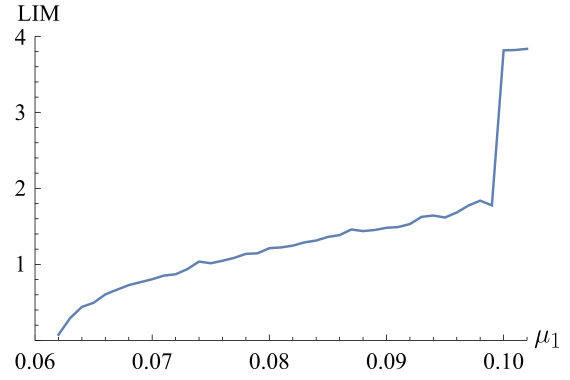

(b) Local integrity measure values while varying the negative damping ratio $\mu_1$.

**Fig. 4** Results of the parameter continuation for the Duffing-Van der Pol oscillator with an attached tuned mass damper; parameter values are as in Table 1

- `discr`: the phase space is divided into a number of cells in each direction based on the value of `discr`.
- `NT`: this indicates the number of points ($N_{\mathrm{T}}$) at which the limit cycle is discretised. The LIM of the solution is assessed through the dynamical integrity of these fixed points, as illustrated in Fig. 2.
- `tfinal`: this parameter specifies the available time for each simulation. If a trajectory does not reach any attractor within this time frame (or if the algorithm fails to classify it), either the user has to manually indicate whether the trajectory is converging to the desired solution, or the algorithm may automatically classify it as non-converging, based on additional settings in the `DynIn` Toolbox.
- `rep_fix_point` determines the minimum number of consecutive points a trajectory must occupy in the same cell for the algorithm to assume it has reached a previously unknown fixed point.
- `rep_periodic`: this specifies the number of times a trajectory must pass through the same cell (but not consecutively) for the algorithm to conclude that it has reached a previously unknown periodic solution.

For each subsequent value of $\mu_1$, a point from the previous limit cycle was used to identify the next one, except for the initial $\mu_1$. The algorithm described in Section 2.1.1 was implemented to identify the limit cycles accurately.

The trend of the LIM as a function of the parameter $\mu_1$ is illustrated in Fig. 4b. The stable limit cycle ceases to exist due to a fold bifurcation for $\mu_1 < 0.0619$, rendering any analysis in that parameter range irrelevant. As shown in Fig. 4b, the LIM is practically zero (approximately 0.07) at $\mu_1 = 0.062$. As $\mu_1$ increases, the LIM rises until approximately $\mu_1 = 0.1$. At this point, it experiences a sudden jump upward, corresponding with the Andronov-Hopf bifurcation of the trivial solution, at which the periodic solution becomes globally stable. Given that the robustness of the stable limit cycle is constrained by the unstable limit cycle, the observed increase in the LIM, as depicted in Fig. 4b, aligns with expectations. Despite the global stability of the limit cycle for $\mu_1 > 0.1005$, the estimated LIM remains finite due to the bounded nature of the considered portion of the phase space. It is important to note that near the Andronov-Hopf bifurcation, the BoA of the trivial equilibrium is already quite small, causing the algorithm to miss its identification. Consequently, the jump in the LIM value occurs slightly before the bifurcation, specifically at $\mu_1 = 0.1$, though the equilibrium loses stability for $\mu_1 > 0.1005$. This issue could be addressed by appropriately tuning the param-

**Table 2** Parameter values of the `DynIn` Toolbox used for the Duffing-Van der Pol oscillator with an attached TMD

| Input | Description | Value |
|---|---|---|
| `number_of_steps` | No. of iteration steps | 1000 |
| `spaceboundary` | Boundary of interest | $x_1 \in [-4, 4]$<br>$x_2 \in [-4, 4]$<br>$\dot{x}_1 \in [-4, 4]$<br>$\dot{x}_2 \in [-4, 4]$ |
| `discr` | No. of cells of the phase space in each direction | 701 |
| `NT` | No. of discretized points of the limit cycle ($N_\mathrm{T}$) | 20 |
| `tfinal` | max. time units of each simulation | 2000 |
| `rep_fix_point` | No. of repetition in a cell before a new fixed point is defined | 400 |
| `rep_periodic` | No. of repetition in a cell before a new periodic sol. is defined | 100 |

eters of the algorithm; however, from a practical standpoint, the problem is considered minor in this case.

## 3.2 Flutter-based energy harvesting wing profile

The second model is a flutter-based energy harvesting wing profile [28–31]. The mechanical model of the system is illustrated in Fig. 5. The planar wing model has two degrees of freedom (DoF), allowing for both pitching ($\alpha$) and plunging ($h$) motions [31–34]. The pitching angle is defined as the angle between the line that connects the aerodynamic (AC), elastic (EC) and gravity (GC) centre of the wing profile and the horizontal axis. The distance between the AC and GC is denoted as $e$. The plunge motion refers to the heave of the EC. The semi-chord of the wing profile is denoted by $b$, and its lifting surface is represented by $S$. The mass, static moment, and moment of inertia of the wing are represented by $M$, $S_\alpha$ and $I_\alpha$, respectively. The airfoil is suspended using a linear longitudinal spring, a nonlinear torsional spring, and both torsional and longitudinal dampers, which serve as power take-off devices. The stiffness of the linear longitudinal spring is denoted as $k_h$, while the stiffness of the nonlinear torsional spring exhibits first, third, and fifth-degree dependencies on the pitch, represented by stiffness coefficients $k_\alpha$, $k_{\alpha 3}$, and $k_{\alpha 5}$. The longitudinal and torsional damping ratios are represented by $c_h$ and $c_\alpha$, respectively. The fluid density around the wing is symbolised as $\rho$, and the lift coefficient slope at zero angle of attack is denoted by $\mathrm{d}C_l$. The aerodynamic moment is $M_a$, and the lift force at the AC is represented by $L$.

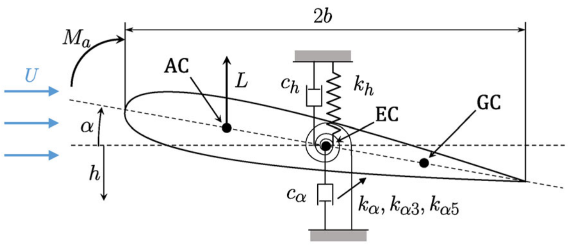

**Fig. 5** Mechanical model of the wing profile

If exposed to sufficiently fast airflow $U$, the profile may experience self-excited flutter oscillations. While this oscillatory motion is typically undesirable for aircraft wings, bridges, and other structures not meant to oscillate, it is a desired motion for energy harvesting applications [30]. The dynamics of the system is governed by the following dimensionless equations of motion [31]:

$$\begin{cases} \ddot{y} + x_\alpha \ddot{\alpha} + (\zeta_h + \beta u)\dot{y} + \Omega^2 y + \beta u^2 \alpha = 0, \\ x_\alpha \ddot{y} + r_\alpha^2 \ddot{\alpha} - \nu u \dot{y} + \zeta_\alpha \dot{\alpha} + (r_\alpha^2 - \nu u^2)\alpha \\ \quad + \xi_{\alpha 3}\alpha^3 + \xi_{\alpha 5}\alpha^5 = 0, \end{cases} \tag{2}$$

where $y = h/b$ represents the dimensionless plunge of the EC. The dimensionless inertia coefficients of the wing are $x_\alpha = S_\alpha/(Mb)$ and $r_\alpha = \sqrt{I_\alpha/\left(Mb^2\right)}$. The dimensionless airflow velocity is $u = U\sqrt{I_\alpha}/\left(b\sqrt{k_\alpha}\right)$, and the frequency ratio is given by $\Omega = \sqrt{k_h I_\alpha/(M k_\alpha)}$. The dimensionless aerodynamic parameters are defined as $\nu = \rho S e \mathrm{d}C_l/(2M)$ and $\beta = \rho S b \mathrm{d}C_l/(2M)$, while the dimensionless damping ratios are represented by $\zeta_\alpha = c_\alpha \sqrt{I_\alpha}/\left(Mb^2\sqrt{k_\alpha}\right)$ and $\zeta_h = c_h\sqrt{I_\alpha}/\left(M\sqrt{k_\alpha}\right)$, relating to pitch and plunge motions, respectively. Lastly, the dimensionless nonlinear torsional stiffnesses are given by $\xi_{\alpha 3} = k_{\alpha 3} I_\alpha/\left(Mb^2 k_\alpha\right)$ and $\xi_{\alpha 5} = k_{\alpha 5} I_\alpha/\left(Mb^2 k_\alpha\right)$. For further details about the model and its parameters, please refer to [34].

The adopted parameter values are presented in Table 3. The parameters varied in this analysis are the dimensionless airflow $u$ and the cubic stiffness $\xi_{\alpha 3}$, which are thus omitted from the table. We note that these parameter values do not represent any specific system; instead, they have been chosen to yield dynamical phenomena that are interesting for the analysis.

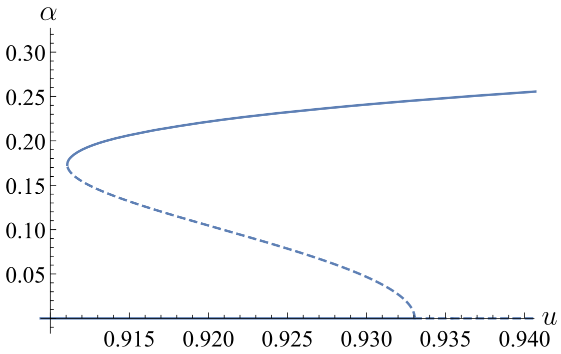

(a) Bifurcation diagram. The amplitude of stable and unstable solutions are denoted by solid and dashed lines, respectively.

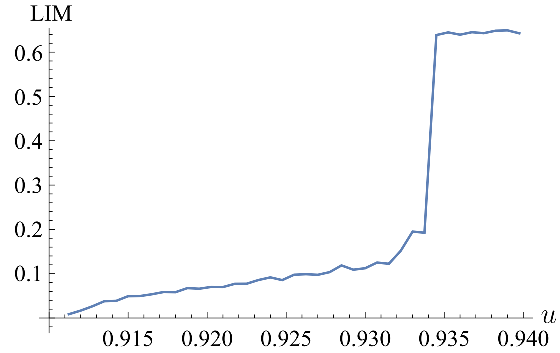

(b) Local integrity measure values while varying the dimensionless airflow $u$.

**Fig. 6** Results of the parameter continuation for the flutter-based energy harvester wing profile

Figure 6a illustrates the bifurcation diagram with the dimensionless airflow $u$ as the bifurcation parameter, while $\xi_{\alpha 3} = -1$. Similarly to the previous system, there is a range of parameters, $u \in [0.911, 0.933]$, where two attractors coexist, separated by an unstable limit cycle. The trivial equilibrium loses its stability around $u = 0.933$ due to an Andronov-Hopf bifurcation. Moreover, the branch of stable periodic solutions merges with the branch of unstable limit cycles at $u = 0.911$ through a fold bifurcation. Since the stable limit cycle and the trivial equilibrium are separated by the unstable limit cycle, the BoA of the stable limit cycle is expected to increase as the distance between the two limit cycles grows. Suppose the shape of the BoA is regular, and there are no other solutions besides the ones in the bifurcation diagram in Fig. 6a, we expect that the trend of the LIM is related to the distance of the limit cycles. Given the similarities in the bifurcation diagram with the system studied in the previous section, we anticipate that the LIM value for the limit cycle will be zero at the fold bifurcation. It is expected to steadily increase until the Andronov-Hopf bifurcation, where it will jump to a higher value as the limit cycle becomes globally stable. However, the presence of other attractors that are not accounted for in the bifurcation analysis could alter this scenario.

The `DynIn` Toolbox's parameter values used for this computation are outlined in Table 4, with their meanings explained in Sect. 3.1. The results of the analysis for $u \in [0.9112, 0.9398]$ and $\xi_{\alpha 3} = -1$, as shown in Fig. 6b, confirm our expectations discussed in the paragraph above. At $u = 0.9112$, near the fold bifurcation, the LIM value is nearly zero, 0.0087. As the value of $u$ increases, the LIM value also increases. When reaching the Andronov-Hopf bifurcation at $u = 0.933$, the slope of the curve becomes noticeably steeper, but a sharp jump in the LIM value occurs only at $u = 0.9345$.

**Table 3** Dimensionless parameter values used for the wing profile

| $x_\alpha$ | $r_\alpha$ | $\beta$ | $\nu$ | $\Omega$ | $\zeta_\alpha$ | $\zeta_h$ | $\xi_{\alpha5}$ |
|---|---|---|---|---|---|---|---|
| 0.2 | 0.5 | 0.2 | 0.08 | 0.5 | 0.01 | 0.01 | 20 |

**Table 4** Parameter values of the `DynIn` Toolbox used for the flutter-based energy harvester wing profile

| Input | Description | Value |
|---|---|---|
| `number_of_steps` | No. of iteration steps | 1000 |
| `spaceboundary` | Boundary of interest | $y \in [-1, 1]$<br>$\alpha \in [-4, 4]$<br>$\dot{y} \in [-1, 1]$<br>$\dot{\alpha} \in [-4, 4]$ |
| `discr` | No. of cells of the phase space in each direction | 1501 |
| `NT` | No. of Poincaré sections per period ($N_\mathrm{T}$) | 20 |
| `tfinal` | Max. time units of each simulation | 5000 |
| `TS` | Sampling time | 2 |
| `rep_fix_point` | No. of repetition in a cell before a new fixed point is defined | 1000 |
| `rep_periodic` | No. of repetition in a cell before a new periodic sol. is defined | 300 |

The discrepancy between the location of the jump in LIM value and of the Andronov-Hopf bifurcation is associated with the extremely slow dynamics experienced very close to the Andronov-Hopf bifurcation, where the trivial solution is almost a centre. This slow dynamics can confuse the algorithm, making it unable to distinguish between trajectories converging to or diverging from the origin. Trajectories that spiral very slowly can mistakenly cause the algorithm to identify nonexistent periodic solutions or fixed points. Although appropriate parameter tuning can help mitigate this issue, as discussed below, it significantly increases computational time. This scenario is challenging to manage even with more sophisticated numerical methods, such as the cell-mapping method [35,36].

Several parameter values were modified compared to the previous example, to avoid misidentifying equilibrium points or periodic orbits. Specifically, the `discr` parameter was increased to reduce the cell dimension, `TS` was raised to increase the sampling time between points on a trajectory, and finally `rep_fix_point` and `rep_periodic` were increased to require a larger number of repetitions to mark a point or a set of points as an equilibrium or periodic orbit, respectively. Since these modifications typically lead to increased computational time, they should only be adjusted as much as necessary. As of now, no specific strategy has been established for optimally tuning these parameters; it largely depends on the user's experience and some carefully chosen default values.

The dynamical integrity of the limit cycle was also analysed concerning the dimensionless cubic stiffness $\xi_{\alpha3}$. The results are presented in Fig. 7. The stability of the linearised system around the trivial equilibrium point does not depend on the coefficients of higher-order terms; therefore, the location of the Andronov-

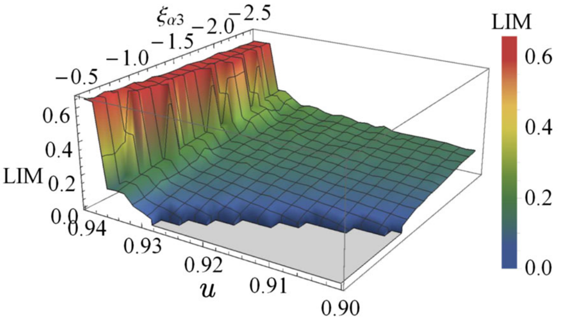

**Fig. 7** Results for the two-dimensional parameter mapping in $(u, \xi_{\alpha 3})$ space of the LIM for the wing profile

Hopf bifurcation remains independent of $\xi_{\alpha 3}$. This observation is supported by the noticeable jump in the LIM value shown in Fig. 7, which occurs at approximately the same airflow $u$ for all values of $\xi_{\alpha 3}$. Therefore, according to Fig. 7 and our observations about the attractors of the system, we conclude that the stable limit cycle becomes globally stable at the same airflow, regardless of the cubic stiffness. However, the parameter region in which the stable limit cycle exists is strongly related to higher-order nonlinear terms through the location of the fold bifurcation. According to the bifurcation diagram in Fig. 6a, this occurs around $u = 0.911$ for $\xi_{\alpha 3} = -1$, and varies with $\xi_{\alpha 3}$, as illustrated in Fig. 7. From Fig. 7, we can see that greater negative values of $\xi_{\alpha 3}$ shift the fold bifurcation to lower airflows. Additionally, the analysis shows that as $\xi_{\alpha 3}$ decreases, the LIM value, representing dynamical integrity, increases. Therefore, both the bistable intervallum and the dynamical integrity increase as the absolute value of the negative $\xi_{\alpha 3}$ increases. Nonetheless, the overall bifurcation scenario remains qualitatively unchanged despite variations in $\xi_{\alpha 3}$.

## 4 Case studies for periodically excited systems

The algorithm has been tested on two case studies involving harmonically excited systems. The first case study examines a Duffing oscillator, and the second regards a nonsmooth system that simulates vertical hopping motion, where the harmonically oscillating ground compensates the lost energy caused by inelastic impacts. For the Duffing oscillator, the results are validated by reformulating the problem as an autonomous system. This is achieved by treating time $t$ as a state variable. The LIM value is then calculated using the algorithm designed for autonomous systems, as discussed in Sect. 3.

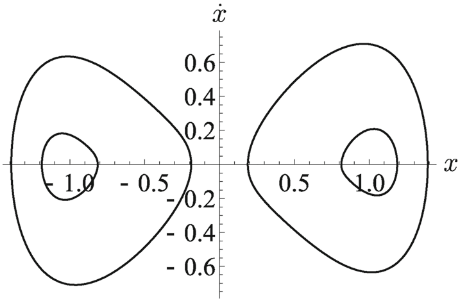

**Fig. 8** Stable periodic orbits of the excited Duffing oscillator for parameters introduced in Table 5

### 4.1 Harmonically excited Duffing oscillator

We examine a harmonically excited Duffing oscillator with negative linear and positive cubic stiffness, resulting in a classical double potential well system. The dynamics of the system is described by the following equation of motion:

$$\ddot{x} + 2\zeta\dot{x} - ax + bx^3 = \gamma\,\cos(\omega t), \tag{3}$$

where $\zeta$ represents the damping ratio, while $a$ and $b$ denote the linear and cubic stiffness coefficients, respectively. Additionally, $\gamma$ and $\omega$ correspond to the amplitude and frequency of the external excitation. The parameter values employed in this analysis are summarized in Table 5. Under these conditions, the system exhibits four stable periodic solutions, which are illustrated in Fig. 8.

The parameter values listed in Table 6 were utilised for the dynamical integrity analysis. We acknowledge that we did not investigate the potential existence of other solutions outside the phase space area defined by the `spaceboundary` values. However, we do not expect that other solutions exist for the specified parameter values. The dynamical integrity analysis is performed on the attractors shown on the right side of Fig. 8. The symmetry of the system allows us to extend the results to the attractors on the left-hand side of the potential well. Since the module for periodically excited periodic orbits is employed, the `NT` input in Table 6 specifies the number of discretised excitation phases. The dynami-

**Table 5** Parameters of the excited Duffing oscillator

| $\zeta$ | $a$ | $b$ | $\gamma$ | $\omega$ |
|---|---|---|---|---|
| 0.15 | 1 | 1 | 0.2 | 0.95 |

**Table 6** Parameter values of the `DynIn` Toolbox used for the harmonically excited Duffing oscillator

| Input | Description | Value |
|---|---|---|
| `number_of_steps` | No. of iteration steps | 200 |
| `spaceboundary` | Boundary of interest | $x \in [-3, 2]$<br>$\dot{x} \in [-2, 3]$ |
| `discr` | No. of cells of the phase space in each direction | 701 |
| `tfinal` | Max. time units of each simulation | 2000 |
| `NT` | No. discretized excitation phases ($N_\mathrm{T}$) | 20 |

cal integrity of the fixed points of the periodic orbit is examined as discussed in Sect. 2.3.2.

The system was analysed over the $\omega \in [0.2, 2]$ parameter range. Due to the nonlinearity of the system, solutions within this frequency range were identified using a sweep-up and a sweep-down approach for the excitation frequency [37–39]. The in-well dynamics exhibits a softening behaviour [40], as seen in the frequency response diagram in Fig. 9, where $\Delta x$ is the peak-to-peak distance of the oscillations. Superharmonic resonance peaks are observed in the frequency response diagram around $\omega = 0.69$ and $\omega = 0.44$, which correspond to approximately half and a third of the natural frequency $\omega_\mathrm{n}$ at the non-trivial steady-state solution of the linearized system, respectively. The non-excited equation of motion has three steady-state solutions: $x_1 = 0$ and $x_{2,3} = \pm\sqrt{a/b}$. The linearized form of (3), centered around $x_2 = \sqrt{a/b}$ is:

$$\ddot{x} + 2\zeta\dot{x} + 2ax - 2a\sqrt{a/b} = \gamma\,\cos(\omega t). \tag{4}$$

By substituting the value of $a$ from Table 5, the natural frequency of the linear system is calculated as $\omega_\mathrm{n} = \sqrt{2a} = \sqrt{2}$.

Based on the diagrams in Figs. 8 and 9, for $\omega \in [0.873, 1.102]$, the system has four stable periodic solutions. Among these, the two pairs of stable periodic solutions are symmetric. At the first fold bifurcation, denoted as a blue triangle in Fig. 9, approximately at $\omega = 1.102$, the inner orbits cease to exist. The second fold bifurcation, represented as an orange circle, occurs around $\omega = 0.873$. Only the lower amplitude orbits exist for frequencies where $\omega < 0.873$. For the parameter values investigated, no stable inter-well solution was identified within the boundary of interest.

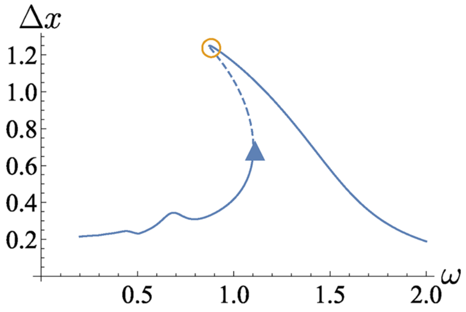

**Fig. 9** Frequency response of the Duffing oscillator. A blue triangle denotes the first fold bifurcation, while an orange circle denotes the second. Stable and unstable branches are represented by solid and dashed lines, respectively

The dynamical integrity was analysed through both sweep-up and sweep-down over the frequency range of $\omega \in [0.2, 2]$ with $\Delta\omega = 0.025$ increments. However, it is important to note that the LIM estimation algorithm does not utilize the continuation, except to identify the periodic orbit. The results are presented in Fig. 10.

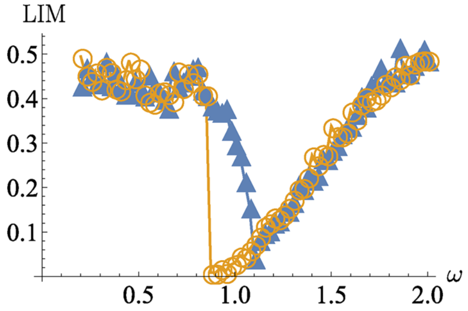

**Fig. 10** Estimated LIM of the forced Duffing oscillator acquired from the sweep-up and sweep-down processes, indicated by blue triangles and orange circles, respectively

During the sweep-up, indicated by blue triangles, the `DynIn` Toolbox followed the inner right periodic solution. The LIM began to decrease steeply at $\omega = 0.95$ as the amplitude of the periodic orbit rapidly increased, as shown in Fig. 9. At $\omega = 1.1$, a cusp is observed in the LIM curve due to the disappearance of the inner solution, which prompts the algorithm to examine the LIM of the outer solution, which becomes the only stable solution in the right potential well. As $\omega$ continues to increase, the LIM value rises because the amplitude of the periodic solution diminishes, as shown in Fig. 9, requiring larger perturbations to diverge toward the left potential well.

During the sweep-down (Fig. 10), the LIM value decreases with the decreasing frequency, closely following the path established by the blue triangles during the sweep-up process. The differences between the two curves are solely due to the numerical approximations of the algorithm. The `DynIn` Toolbox managed to track the outer orbit until $\omega = 0.875$, at which point the LIM approached nearly zero as the algorithm neared the fold bifurcation denoted by an orange circle in Fig. 9. As the frequency decreases further, the LIM value experiences a sudden positive jump as the algorithm identifies the inner periodic solution, which becomes the only in-well solution in the right potential well. For lower values of $\omega$, variations in the LIM are minimal, reflecting the marginal changes in the amplitude of the periodic solution.

The determined LIM estimates are validated by calculating the actual BoA of the system at three $\omega$ values describing the three qualitatively different behaviors of the system. The BoA is determined in five equidistant phases, as shown in Fig. 11. The BoA of the small and big amplitude solutions in the left potential well are denoted by orange and yellow colours, whereas those of the small and big amplitude solutions of the right potential well are marked by blue and green colours, respectively. At $\omega = 0.7$, only the two small-amplitude periodic orbits exist. In the related Fig. 11a, the examined rightmost periodic orbit is shown. The sections of the hypertorus, with radius determined by the `DynIn` Toolbox, are denoted by red circles. The smaller LIM value is used as the radius since both at sweep up and down the same periodic orbit was examined, and the `DynIn` Toolbox offers an upper estimate of the dynamical robustness. As shown, the hypertorus grazes the BoA borders, which confirms the accuracy of the estimation algorithm.

At $\omega = 1$, all four periodic orbits shown in Fig. 8 exist. Therefore, two examined hypertories are shown in Fig. 11b : one related to the large amplitude solution (the periodic orbit is referred to by a dashed black line) and one to the small amplitude one (a solid black line). Both hypertories graze their respective BoA, which validates the algorithm also in this case. We note that the LIM of the large amplitude solution is very small, making the sections of the relative hypertorus not easily recognizable.

In Fig. 11c, for $\omega = 1.3$, only the two large amplitude orbits exist. The rightmost periodic orbit is referenced by a dashed line. Here, just as with the previous ones, the hypertorus grazes the border of the BoA. Therefore, we assume that the LIM values are correct also for all other $\omega$ values, since the shapes of the BoA are regular and the behavior of the system qualitatively falls under one of the three examples.

#### 4.1.1 Autonomous form of the harmonically excited Duffing oscillator

To verify the results of the dynamical integrity analysis presented in Sect. 4.1, we reformulated the harmonically excited Duffing oscillator into an autonomous form by incorporating time $t$ as one of the state variables. The equation of motion for the system in the extended state space is given by:

$$\begin{cases} x'' + 2\zeta x' - ax + bx^3 = \gamma \cos(\omega t), \\ t' = 1. \end{cases} \tag{5}$$

Since all state variables $\mathbf{z} = [x, x', t]^{\mathrm{T}}$ have to be periodic for the `DynIn` Toolbox to function appropriately,

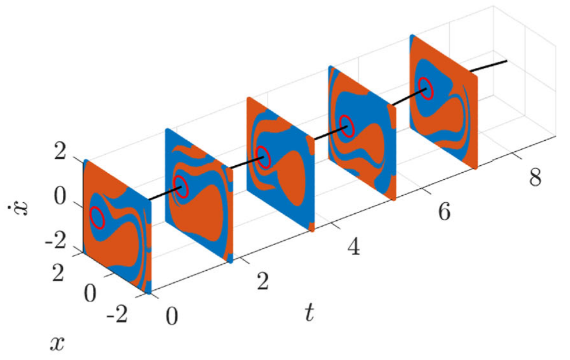

(a) BoAs at $\omega = 0.7$.

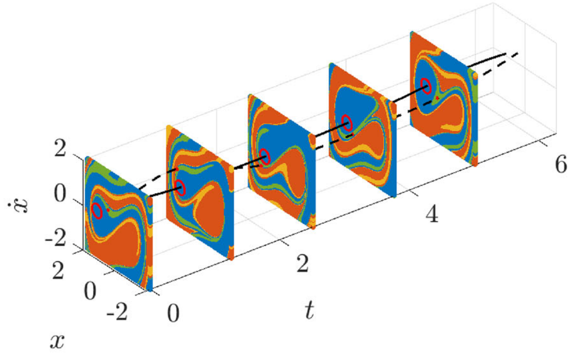

(b) BoAs at $\omega = 1$.

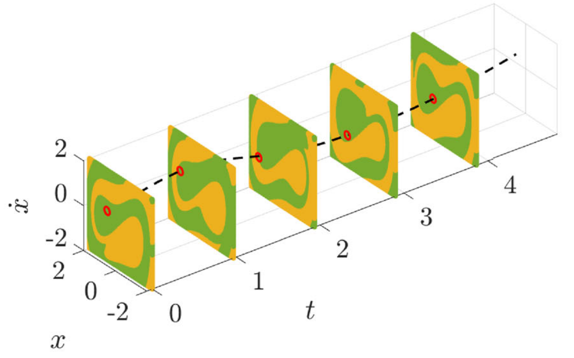

(c) BoAs at $\omega = 1.3$.

**Fig. 11** Comparision of the actual BoAs with the LIM calculated by the `DynIn` Toolbox for the system in Eq. (3). The periodic orbits are denoted by black lines, the sections of the hypertories are denoted by red circles

we map time such that $t \mapsto t_0$ when $t = t_0 + T$, where $T$ is the period and $t_0$ is chosen arbitrarily. This transformation results in a nonsmooth system, with the event defined as $h(\mathbf{z}) = 0$ and the corresponding mapping defined by $\mathbf{g}(\mathbf{z}_{\text{in}}) \mapsto \mathbf{z}_{\text{out}}$. The event function is given as:

$$h(t) = t - t_0 - T, \tag{6}$$

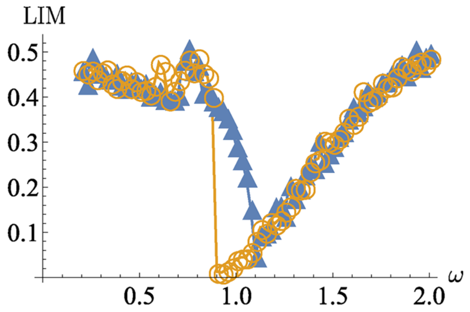

**Fig. 12** Estimated LIM of the autonomous Duffing oscillator acquired by sweep-up and sweep-down denoted by blue triangles and orange circles, respectively

furthermore, the mapping function is expressed as:

$$\mathbf{g}(x, x', t) = [x,\ x',\ t_0]^{\mathrm{T}}. \tag{7}$$

The event function was detected using the event handler of the built-in differential equation solver `ode45` in MATLAB. The extension of the state space does not affect the behaviour of the system discussed in Sect. 4.1. The system was analysed using the algorithm described in Sect. 2.3.1.

The dynamical integrity analysis was conducted using sweep-up and sweep-down methods within the parameter range $\omega \in [0.2, 2]$. The results are illustrated in Fig. 12. For both the sweep-up and down processes, the `DynIn` module for autonomous systems provided estimations for the LIM values that were approximately identical to those obtained in Sect. 4.1. Furthermore, the algorithm successfully switched between the two periodic orbits at the same $\omega$ values as when the system was treated as non-autonomous. In conclusion, the results realised in Sect. 4.1 are presumed to be correct. Moreover, this analysis proved that the module of the `DynIn` Toolbox designed for limit cycles is able to handle nonsmooth systems.

### 4.2 Vertical hopping model

A two-degrees-of-freedom vertical hopping system is analysed [41,42]. The model consists of an upper and a lower body (two lumped masses) connected by a spring, hopping on a moving ground, as illustrated in Fig. 13. During the hopping motion, the system loses energy upon touchdown due to the assumption of a perfectly inelastic impact. This lost energy is restored by the har-

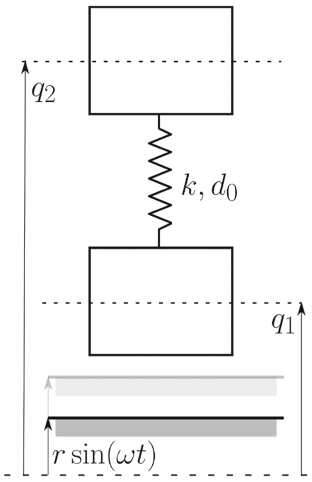

**Fig. 13** Mechanical model of vertical hopping on harmonically oscillating ground

monically oscillating ground, allowing for stable periodic motions of the system. This setup is analogous to the one introduced in [41]. The nonsmooth nature of the system results in two distinct phases that govern the motion: the flight and stance phases. During the flight phase, when the model is not in contact with the ground, it is influenced only by the elastic force between the two masses and the gravitational force. The dimensionless equations of motion for the flight phase are given by

$$\begin{cases} z_1'' - z_2 + z_1 + 1 + \gamma = 0, \\ z_2'' + M(z_2 - z_1 - 1) + \gamma = 0, \end{cases} \tag{8}$$

where the prime ($'$) denotes differentiation with respect to the dimensionless time $\tau = t\sqrt{k/m_1}$, with $m_1$ as the mass of the lower body and $k$ as the spring stiffness. The state variables $z_1 = q_1/d_0$ and $z_2 = q_2/d_0$ represent the dimensionless elevation of the lower and upper masses, respectively, normalised by the unloaded spring length $d_0$. The mass ratio between the bodies is represented by $M = m_1/m_2$, and $\gamma = gm_1/(d_0 k)$ is the dimensionless gravity coefficient. The event function $h_{\mathrm{F2S}} = 0$ represents the transition from the flight to the stance (F2S) phase, occurring when the lower mass contacts the oscillating ground. It is expressed as

$$h_{\mathrm{F2S}} = z_1 - z_{\mathrm{gr}}, \tag{9}$$

where $z_{\mathrm{gr}}$ denotes the harmonic motion of the ground, represented by

$$z_{\mathrm{gr}} = \rho \sin(2\pi\phi\tau), \tag{10}$$

with $\rho = r/d_0$ being the normalised amplitude of ground oscillations; the normalised frequency of ground oscillations is given by $\phi = f\sqrt{m_1/k}$, where $f$ is the dimensional frequency of ground excitation. After the touchdown, the lower mass moves with the ground until take-off. The mapping function of the state $\mathbf{z} = [z_1, z_2, z_1', z_2']$ at the F2S event is defined as

$$\mathbf{g}_{\mathrm{F2S}} = [z_1,\ z_2,\ z_{\mathrm{gr}}',\ z_2']^{\mathrm{T}}. \tag{11}$$

Therefore, the system has $\mathrm{C}^0$ continuity at the F2S phase transition.

In the stance phase, the governing equations of motion are given by

$$\begin{cases} z_1'' + (2\pi\phi)^2 z_{\mathrm{gr}} = 0, \\ z_2'' + M(z_2 - z_1 - 1) + \gamma = 0. \end{cases} \tag{12}$$

The transition from stance to flight (S2F) occurs when the ground reaction force becomes zero. The corresponding event function $h_{\mathrm{S2F}} = 0$ at take-off is defined as

$$h_{\mathrm{S2F}} = z_1 + 1 + \gamma - (2\pi\phi)^2 z_{\mathrm{gr}} - z_2. \tag{13}$$

At take-off, the mapping function of the state is the identity

$$\mathbf{g}_{\mathrm{S2F}} = [z_1,\ z_2,\ z_1',\ z_2']^{\mathrm{T}}, \tag{14}$$

since the non-smoothness only affects accelerations. We encourage interested readers to refer to the original model and equations in [41] for further details.

During the dynamical integrity analysis, we focused on periodic orbits with periods of $\tilde{T} = 1/\phi$. Impacts between the two masses were considered an unacceptable condition. Therefore, a trajectory that included an impact between the masses was deemed nonconvergent. This assumption reflects a common practical condition where, despite having only one stable solution, certain transient conditions are unacceptable and effectively limit the dynamical integrity of that stable solution. We note that simulations do not terminate

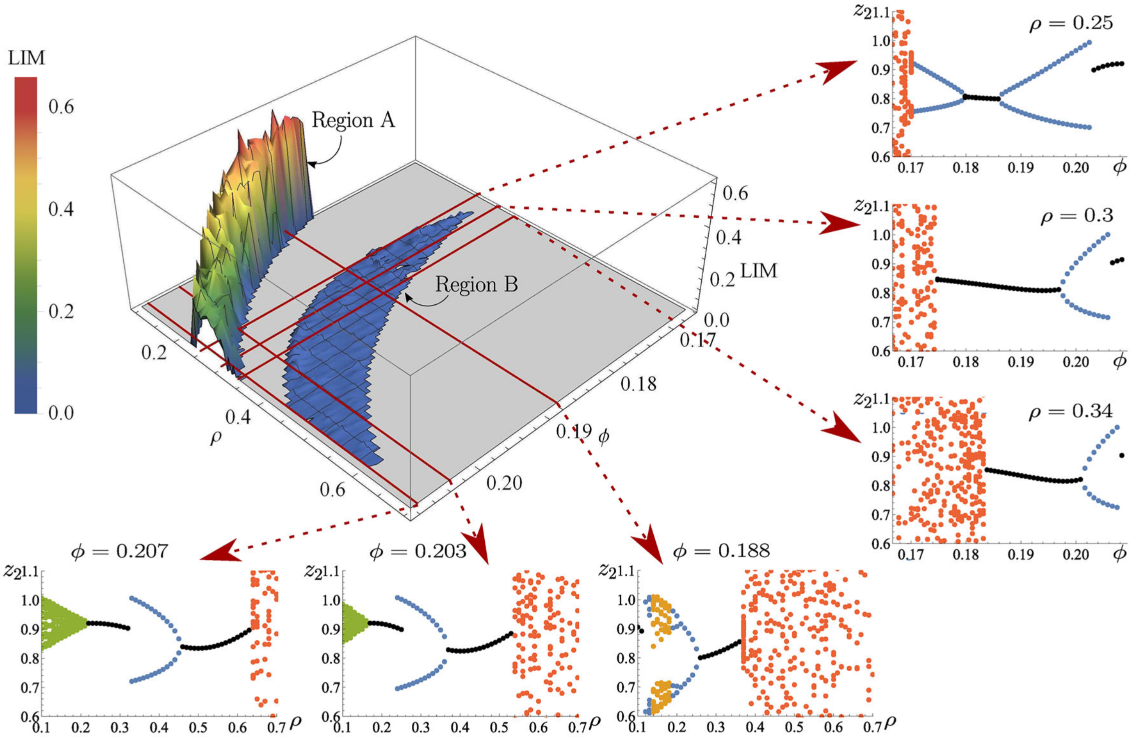

**Fig. 14** Results for the vertical hopping model. The main figure shows the estimated LIM value for period $\tilde{T}$ orbits. The cross-sections illustrate points of stable periodic motions at the Poincaré section $\tau = \kappa/\phi$, where $\kappa \in \mathbb{N}$; in the cross-sections, single points (black dots) correspond to a period $\tilde{T}$ orbit, two or more points indicate either periodic solutions with higher period (blue dots), quasiperiodic (green dots), or chaotic solutions (orange dots)

**Table 7** Parameter values of the vertical hopping model

| $M$ | $\gamma$ |
|---|---|
| 1 | 0.08 |

upon collision; collisions are identified in subsequent analysis.

The parameter values used in the analysis are presented in Table 7. The dynamical integrity analysis was conducted for variations in the excitation frequency $\phi$ and amplitude $\rho$, which is why these parameters are not included in the table.

The parameter values of the `DynIn` Toolbox are displayed in Table 8. Since the oscillating floor constrains the phase space of physically feasible initial conditions, if the algorithm selects an IC that would place the lower mass below the current ground level, the initial condition $\mathbf{z}_0$ will be adjusted according to (11).

The LIM values in the $(\rho, \phi)$ plane are illustrated in Fig. 14 along with frequency responses for various sections of $\rho$ and $\phi$. Stable orbits with period $\tilde{T}$ exist within two contiguous areas that resemble Arnold tongues in the LIM value diagram; we call these areas 'period-1 regions'. To distinguish between the two areas, one is referred to as region A, the other as region B, as indicated in the figure. The regions containing single period $\tilde{T}$ orbits (denoted by black dots on the frequency response diagrams) are separated by period-doubling domains (referenced by blue dots) alongside both excitation amplitudes and frequencies. For the low excitation amplitude oscillations, like the ones within region A, the lower mass mainly moves with the ground, as shown in Fig. 15, only slightly separating from it for a short time each period. The maximum deviation from the ground in the presented case is about 1% of the excitation amplitude. In contrast, for high excitation amplitudes in region B, the oscillations of both masses become significantly greater than those observed at lower excitation amplitudes in region A. In Fig. 16, the lower mass deviates from the ground by a magnitude of approximately 75% of the excitation amplitude, resulting in the airborne phase comprising three-

**Table 8** Parameter values of the DynIn Toolbox used for the vertical hopping model

| Input | Description | Value |
|---|---|---|
| `number_of_steps` | No. of iteration steps | 500 |
| `spaceboundary` | Boundary of interest | $z_1 \in [-2, 5]$<br>$z_2 \in [-2, 5]$<br>$z_1' \in [-5, 5]$<br>$z_2' \in [-5, 5]$ |
| `discr` | No. of cells of the phase space in each direction | 701 |
| `tfinal` | Max. time units of each simulation | 2000 |
| `NT` | No. discretized excitation phases ($N_\mathrm{T}$) | 20 |

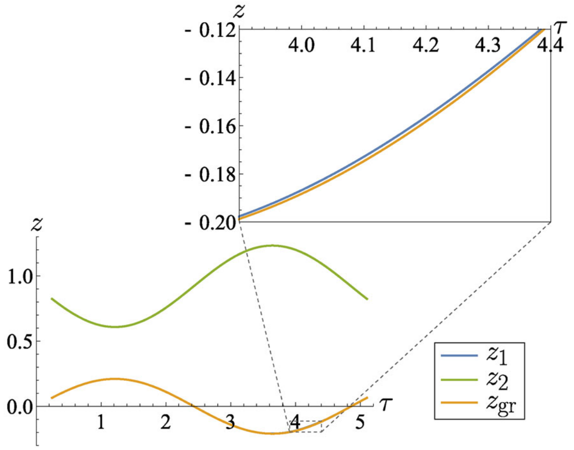

**Fig. 15** A hopping period for $\rho = 0.21$ and $\phi = 0.206$. The lower mass has only a minimal detachment from the ground, visible in the inset

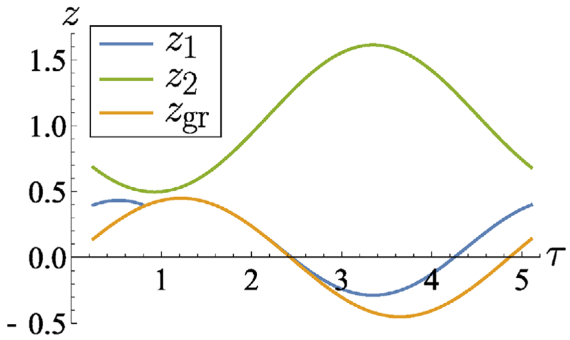

**Fig. 16** A hopping period for $\rho = 0.45$ and $\phi = 0.206$.

quarters of the period. In the case of period doubling motions, the lower mass mainly moves with the ground in one period and has great oscillations in the consecutive one (the corresponding figure is omitted, as period doubling motions are not the subject of the analysis).

At even higher excitation amplitudes $\rho$, chaotic behaviour is observed in the frequency response diagram, as shown by dark orange dots in the lower three figures of Fig. 14. As the excitation frequency increases, the chaotic behaviour shifts to higher $\rho$ values, as shown in the three diagrams from right to left.

Regarding the amplitude cross-sections displayed in the right column in Fig. 14, the chaotic behaviour (indicated by dark orange dots) occurs at low frequencies. As the excitation amplitude increases, this chaotic behaviour shifts to higher frequencies, as illustrated in the right column from top to bottom. The chaotic solutions observed at both high excitation amplitudes and low frequencies are not physical, as the upper mass crosses over the lower mass, even going below ground level.

Notably, in the $\phi = 0.188$ frequency cross-section, the period doubling behaviour also transitions to chaotic behaviour, referred to by light orange dots, while decreasing the $\rho$ value. In contrast to the chaotic behaviours denoted by dark orange dots, here the realised motion is feasible, since the masses do not collide during motion. Interestingly, as the excitation amplitude decreases even more, a period $\tilde{T}$ motion occurs. A similar pattern is noticeable in the $\rho = 0.25$ amplitude cross-section, where a distinguishable period doubling behaviour occurs for a significantly large region $\phi \in [0.17, 0.186]$ prior to the onset of chaos; however, no synchronisation ensues in this case by further decreasing $\phi$.

Conversely, the frequency cross-sections at the bottom row in Fig. 14 indicate that the system exhibits quasiperiodic solutions at very low excitation amplitudes, denoted by green dots. At higher frequencies, the quasiperiodic behaviour shifts to higher amplitudes.

According to the frequency cross-section for $\phi = 0.207$ two domains with a single period $\tilde{T}$ exist, specifically within $\rho \in [0.21, 0.32]$ and $\rho \in [0.45, 0.63]$. However, the LIM was not calculated for the latter $\rho$ range (as indicated by the gray area bordering region B) because the masses collide during periodic motion under those parameters, which we have categorized as a non-designated operation. Therefore, no LIM value is assigned for those periodic orbits. Nevertheless, there were no collisions of the masses for smaller $\phi$ values, although the LIM values are very small, as marked by the blue area in Fig. 14. The maximum LIM value in region A is 0.62, whereas in region B it is only 0.04.

At the $\phi = 0.203$ cross-section diagram for $\rho \in [0.24, 0.25]$, bistable behaviour is observed with single and double $\tilde{T}$ period motions. The output of the `DynIn` Toolbox at excitation amplitude $\rho = 0.24$ is shown in Fig. 17. The value of LIM is represented by the magnitude of the red circles' radius around the single period orbit's sampling points, indicating the projection of the hyperspheres onto $(z_2, z_2')$. The `DynIn` Toolbox was able to identify the period doubling solution, referred to by blue dots. At the bistable region the dynamical integrity is defined by the other attractor rather than the collision of the masses.

Overall, the dynamical integrity is much larger for the period-1 region A, as clearly visible in Fig. 14. As $\phi$ increases, the occurrence of the quasiperiodic behaviour shifts to higher $\rho$ values, causing solutions with a period $\tilde{T}$ to also move to higher excitation amplitudes. Consequently, the period-1 regions are curved along the $\rho$ axis. Additionally, due to this shifting, at the high-frequency end of the period-1 region A the LIM is smaller. The reason behind this is the curved nature of the region: for the higher frequencies, the amplitude is also increasing for the period-1 region A. Due to the higher $\rho$ values, the distance between the masses reduces during the periodic motion. Therefore, a smaller perturbance is enough for causing a collision. Regarding the period-1 region B, the masses undergo more significant oscillations and tend to approach each other during motion. Therefore, the distance between the lumped masses diminishes, as discussed. Thus, due to perturbations, the likelihood of mass collisions increases, thereby severely limiting the dynamical integrity of the solution. In addition to the lower estimated LIM values, another drawback of region B is the nearby presence of the chaotic domain, as opposed to region A, which is neighboured by quasiperiodic and period-doubling domains. As a result, perturbations in the excitation around this border may also trigger sudden, undesired behaviour.

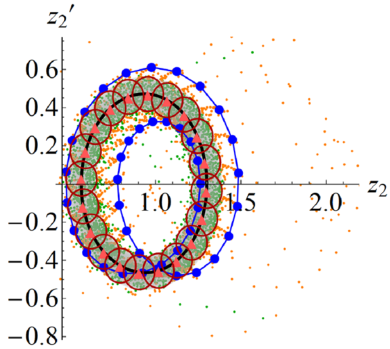

**Fig. 17** Output for vertical hopping model at excitation parameters, $\rho = 0.24$ and $\phi = 0.203$, where the system has bistable behaviour. Solid black curve: examined periodic orbit; red triangles: discretised points of the periodic orbit; grey area: projection of the hypertorus on the phase plane's section $(z_2, z_2')$; green dots: sampling points of converging trajectories, orange dots: sampling points of non-converging trajectories; blue dots: points of other attractor found by the algorithm

## 5 Conclusions

A rapid algorithm, namely the `DynIn` Toolbox, was introduced in [23] to estimate the dynamical integrity of a system's steady-state behaviour using the local integrity measure. The present study enhances the functionality of the Toolbox by extending its applicability to estimating the LIM of periodic orbits, particularly for both autonomous systems and those subjected to periodic excitation. For this purpose, the definition of LIM was adapted to accommodate periodic orbits.

One of the strengths of the `DynIn` Toolbox is its versatility. The iterative algorithm does not necessarily require explicit equations of motion. Instead, it can work with black-box models as long as trajectories in a finite dimensional phase space can be generated, making it a powerful tool for a broad range of applications. The other key advantage of the `DynIn` Toolbox is its speed, which makes it suitable for parametric analysis

– a task that is nearly impossible with traditional BoA analysis methods.

To facilitate precise computations, the Toolbox offers a range of optional inputs. These include parameters such as the cell division density of the state space, time-step size, and simulation tolerances. While default values are provided for these inputs, fine-tuning them is essential, as optimal configurations can vary significantly depending on the specific system under investigation. As discussed in Sect. 3.2, this may be necessary for certain types of systems to ensure robust performance.

In this study, the developed algorithm was showcased through various case studies. In particular, a Duffing-van der Pol oscillator with a TMD and a wing profile were investigated in Sect. 3, while a harmonically excited Duffing oscillator and a two-degrees-of-freedom passive vertical hopping model were studied in Sect. 4. Notably, the Toolbox can manage autonomous and non-autonomous systems and is capable of handling nonsmooth systems for both cases, as highlighted in Sect. 4.1.1 and 4.2, respectively. We note that the algorithm was not applied on systems with strongly intermingled BoA shapes, where basin erosion can play a significant role; this remains a still unexplored topic, which will be the subject of future studies.

The output of the LIM estimations of the `DynIn` Toolbox aligns with the expectations based on bifurcation diagrams, assuming regular shapes in the BoA, therefore validating the robustness and reliability of the algorithm. The Toolbox proves to be convenient, delivering fast dynamical integrity estimations. During the analysis, trajectories are examined and classified based on their behaviour as either converging or non-converging regarding the investigated periodic orbit. As more trajectories are identified, the computational time required for each iteration shortens due to cell subdivision and classification of the investigated state space.

However, it is essential to note that parameter tuning remains a potential bottleneck within the `DynIn` Toolbox. Users should thoroughly examine the output, especially concerning identified new attractors. When convergence speeds are low, there is a risk that the Toolbox may incorrectly classify equilibrium points or periodic solutions, leading to inaccuracies in the results. Additionally, if the BoA of another attractor is minor, there is a chance that the algorithm overlooks it, since the chance of choosing an IC within the BoA is minimal. To mitigate these risks, users can increase the cell division density, time-step size, and cell repetition numbers (a trajectory is assumed to have reached a new attractor if it stays in or passes through the same cell(s) at least a specified number of times), which can reduce the risk of false identification. Conversely, increasing the iteration steps provides a more thorough examination of the state space. However, this comes at the cost of increased memory usage and longer running times. Thus, achieving a balance between precision and computational efficiency is important.

In conclusion, the `DynIn` Toolbox stands out as a flexible and robust numerical algorithm that provides valuable insights into the overall global dynamics, specifically the dynamical integrity of various dynamical systems through the estimation of the LIM. The `DynIn` Toolbox is readily available for download, accompanied by a comprehensive tutorial and example problems to assist users in maximizing its capabilities.

**Author contributions** G.H. wrote the introduction text, D.P. wrote the texts of other sections. D.P. prepared figures 1-3, 4b, 6b, 7-17 and G.H. prepared figures 4a, 5, 6a. All authors reviewed the manuscript.

**Funding** Open access funding provided by Budapest University of Technology and Economics. This research was financially supported by the Hungarian Academy of Sciences (Magyar Tudományos Akadémia) under the Lendület program.

**Data Availability Statement** Not applicable

## Declarations

**Code availability** The data and the code utilized for generating the presented results, including the `DynIn` Toolbox, are freely available at https://gdrg.mm.bme.hu/.

**Conflict of interest** The authors declare that they have no Conflict of interest.

## References

1. Soliman, M.S., Thompson, J.M.T.: Integrity measures quantifying the erosion of smooth and fractal basins of attraction. J. Sound Vib. **135**, 453–475 (1989)
2. Lenci, S., Rega, G.: Global nonlinear dynamics for engineering design and system safety. Springer (2019)
3. Menck, P.J., Heitzig, J., Marwan, N., Kurths, J.: How basin stability complements the linear-stability paradigm. Nat. Phys. **9**(2), 89–92 (2013)
4. Horvath, H.Z., Takacs, D.: Stability and local bifurcation analyses of two-wheeled trailers considering the nonlinear coupling between lateral and vertical motions. Nonlinear Dyn. **107**(3), 2115–2132 (2021). https://doi.org/10.1007/s11071-021-07120-9
5. Kadar, F., Stepan, G., Habib, G.: Model-free fold bifurcation prediction from pre-bifurcation scenario: experimental validation through wheel shimmy vibrations. Nonlinear Dyn. (2025). https://doi.org/10.1007/s11071-024-10686-9
6. Dimitriadis, G.: Introduction to nonlinear aeroelasticity. John Wiley & Sons (2017)
7. Verstraelen, E., Dimitriadis, G., Rossetto, G.D.B., Dowell, E.H.: Two-domain and three-domain limit cycles in a typical aeroelastic system with freeplay in pitch. J. Fluids Struct. **69**, 89–107 (2017). https://doi.org/10.1016/j.jfluidstructs.2016.11.019
8. Ubellacker, W., Csomay-Shanklin, N., Molnar, TG., Ames, A.D.: Verifying safe transitions between dynamic motion primitives on legged robots. In: 2021 IEEE/RSJ International conference on intelligent robots and systems (IROS). IEEE. (2021) https://doi.org/10.1109/iros51168.2021.9636537
9. Settimi, V., Lenci, S., Rega, G.: Combined effect of wind and sea excitations on the internal resonance response of floating offshore wind turbines. Nonlinear Dyn. (2025). https://doi.org/10.1007/s11071-025-10905-x
10. Du, Y., Li, Q., Fan, H., Zhan, M., Xiao, J., Wang, X.: Inferring attracting basins of power system with machine learning. Phys. Rev. Res. **6**(1), 013181 (2024). https://doi.org/10.1103/physrevresearch.6.013181
11. Francomano, E., Hilker, F.M., Paliaga, M., Venturino, E.: Separatrix reconstruction to identify tipping points in an eco-epidemiological model. Appl. Math. Comput. **318**, 80–91 (2018). https://doi.org/10.1016/j.amc.2017.07.022
12. Beisner, B., Haydon, D., Cuddington, K.: Alternative stable states in ecology. Front. Ecol. Environ. **1**(7), 376–382 (2003). https://doi.org/10.1890/1540-9295(2003)001[0376:assie]2.0.co;2
13. Levin, A.: An analytical method of estimating the domain of attraction for polynomial differential equations. IEEE Trans. Autom. Control **39**(12), 2471–2475 (1994). https://doi.org/10.1109/9.362845
14. Genda, A., Fidlin, A., Gendelman, O.: The level-crossing problem of a weakly damped particle in quadratic potential well under harmonic excitation. Nonlinear Dyn. **111**(22), 20563–20578 (2023). https://doi.org/10.1007/s11071-023-08875-z
15. Settimi, V., Saetta, E., Rega, G.: Nonlinear dynamics of a third-order reduced model of thermomechanically coupled plate under different thermal excitations. Meccanica **55**(12), 2451–2473 (2020). https://doi.org/10.1007/s11012-019-01117-w
16. Rega, G., Settimi, V.: Global dynamics perspective on macro- to nano-mechanics. Nonlinear Dyn. **103**(2), 1259–1303 (2021). https://doi.org/10.1007/s11071-020-06198-x
17. Rega, G.: Nonlinear dynamics in mechanics: state of the art and expected future developments. J. Comput. Nonlinear Dyn. **17**(8), 080802 (2022). https://doi.org/10.1115/1.4054112
18. Hsu, C.S.: A theory of cell-to-cell mapping dynamical systems. J. Appl. Mech. **47**(4), 931–939 (1980). https://doi.org/10.1115/1.3153816
19. Hsu, C.S.: Cell-to-cell mapping: a method of global analysis for nonlinear systems, 64. Springer Science & Business Media (2013)
20. Xiong, F.R., Qin, Z.C., Ding, Q., Hernndez, C., Fernandez, J., Schütze, O., Sun, J.Q.: Parallel cell mapping method for global analysis of high-dimensional nonlinear dynamical systems. J. Appl. Mech. **82**(11), 111010 (2015). https://doi.org/10.1115/1.4031149
21. Belardinelli, P., Lenci, S.: An efficient parallel implementation of cell mapping methods for mdof systems. Nonlinear Dyn. **86**(4), 2279–2290 (2016). https://doi.org/10.1007/s11071-016-2849-3
22. Thompson, J.M.T.: Chaotic phenomena triggering the escape from a potential well. Proc. R. Soc. Lond. A Math. Phys. Sci. **421**(1861), 195–225 (1989). https://doi.org/10.1098/rspa.1989.0009
23. Habib, G.: Dynamical integrity assessment of stable equilibria: a new rapid iterative procedure. Nonlinear Dyn. **106**, 1–24 (2021). https://doi.org/10.1007/s11071-021-06936-9
24. Lenci, S., Rega, G.: Optimal control of homoclinic bifurcation: theoretical treatment and practical reduction of safe basin erosion in the helmholtz oscillator. J. Vib. Control **9**(3–4), 281–315 (2003). https://doi.org/10.1177/107754603030753
25. Szaksz, B., Stepan, G., Habib, G.: Dynamical integrity estimation in time delayed systems: a rapid iterative algorithm. J. Sound Vib. **571**, 118045 (2024)
26. Gattulli, V., DiFabio, F., Luongo, A.: Simple and double hopf bifurcations in aeroelastic oscillators with tuned mass dampers. J. Frankl. Inst. **338**, 187–201 (2001)
27. Habib, G., Kerschen, G.: Suppression of limit cycle oscillations using the nonlinear tuned vibration absorber. Proc Royal Soc.: Math., Phys. Eng. Sci. **471**(2176) (2015). https://doi.org/10.1098/rspa.2014.0976
28. Lee, Y.S., Vakakis, A.F., Bergman, L.A., McFarland, D.M., Kerschen, G.: Suppression aeroelastic instability using broadband passive targeted energy transfers, part 1: Theory. AIAA J. **45**(3), 693–711 (2007). https://doi.org/10.2514/1.24062
29. Lee, Y.S., Kerschen, G., McFarland, D.M., Hill, W.J., Nichkawde, C., Strganac, T.W., Bergman, L.A., Vakakis, A.F.: Suppressing aeroelastic instability using broadband passive targeted energy transfers, part 2: Experiments. AIAA

J. **45**(10), 2391–2400 (2007). https://doi.org/10.2514/1.28300

30. Tsushima, N., Su, W.: Modeling of highly flexible multifunctional wings for energy harvesting. J. Aircraft **53**(4), 1033–1044 (2019). https://doi.org/10.2514/1.C033496
31. Habib, G., Horvath, A.: Forecasting fold bifurcations through physics-informed convolutional neural networks. Nonlinear Phenomena, Physica D (2023)
32. Lee, B., Jiang, L., Wong, Y.: Flutter of an airfoil with a cubic nonlinear restoring force. In: 39th AIAA/ASME/ASCE/AHS/ASC Structures, structural dynamics, and materials conference and exhibit (1998). https://doi.org/10.2514/6.1998-1725
33. Pettit, C.L., Beran, P.S.: Effects of parametric uncertainty on airfoil limit cycle oscillation. J Aircraft **40**(5), 1004–1006 (2003). https://doi.org/10.2514/2.6889
34. Malher, A., Touz, C., Doar, O., Habib, G., Kerschen, G.: Flutter control of a two-degrees-of-freedom airfoil using a nonlinear tuned vibration absorber. J. Comput. Nonlinear Dyn. **12**(5), 051016 (2017). https://doi.org/10.1115/1.4036420
35. Vio, G.A., Dimitriadis, G., Cooper, J.E.: Bifurcation analysis and limit cycle oscillation amplitude prediction methods applied to the aeroelastic galloping problem. J. Fluids Struct. **23**(7), 983–1011 (2007)
36. Sun, J.Q., Xiong, F.R., Schtze, O., Hernndez, C.: Cell mapping methods: algorithmic approaches and applications. Springer Singapore (2018). https://doi.org/10.1007/978-981-13-0457-6
37. Rega, G., Lenci, S.: Identifying, evaluating, and controlling dynamical integrity measures in non-linear mechanical oscillators. Nonlinear Anal. Theory Methods Appl. **63**, 902–914 (2005)
38. Koudahoun, H.L., Kpomahou, Y.J.F., Akande, J., Adja, D.K.K.: Chaotic dynamics of an extended duffing oscillator under periodic excitation. World J. Appl. Phys.**3**(2), 34–50 (2018). https://doi.org/10.11648/j.wjap.20180302.13
39. Soares, dL.I., Krol, M.F., Rech, P.C.: Coexisting attractors and basins of attraction of an extended forced duffing oscillator. Eur. Phys. J. B **97**(71), 902–914 (2024). https://doi.org/10.1140/epjb/s10051-024-00709-0
40. Tajaddodianfar, F., Yazdi, M., Pishkenari, H.: Nonlinear dynamics of mems/nems resonators: analytical solution by the homotopy analysis method. Microsyst. Technol. **23**, 1913–1926 (2017). https://doi.org/10.1007/s00542-016-2947-7
41. Dankowicz, H., Piiroinen, P.: Exploiting discontinuities for stabilization of recurrent motions. Dyn. Syst.-an Int. J-DYN SYST **17**, 317–342 (2002). https://doi.org/10.1080/1468936021000041663
42. Zelei, A., Insperger, T.: Simplest mechanical model of stable hopping with inelastic ground-foot impact. IFAC-PapersOnLine **51**(22), 372–377 (2018). https://doi.org/10.1016/j.ifacol.2018.11.570
43. Schilder, F., Peckham, B.B.: Computing Arnold tongue scenarios. Journal of Computational Physics 220(2), 932–951 (2007). https://doi.org/10.1016/j.jcp.2006.05.041